



Programmed degradation of a hierarchical nanoparticle with redox and light responsivity for self-activated photo-chemical enhanced chemodynamic therapy



Shenqiang Wang^{a,b,1}, Letao Yang^{b,1}, Hyeon-Yeol Cho^b, Sy-Tsong Dean Chueng^b, Zhang Hepeng^a, Qiuyu Zhang^{a,*}, Ki-Bum Lee^{b,c,**}

^a MOE Key Laboratory of Material Physics and Chemistry Under Extraordinary Conditions, School of Natural and Applied Sciences, Northwestern Polytechnical University, Xi'an, 710129, China

^b Department of Chemistry and Chemical Biology, Rutgers University, Piscataway, NJ, 08854, USA

^c Department of Life and Nanopharmaceutical Science, College of Pharmacy, Kyung Hee University, Seoul, 02447, South Korea

ARTICLE INFO

Keywords:

Programmed degradation
Tumor microenvironment
Hierarchical nanoparticle
Self-activated chemodynamic therapy
Photothermal therapy
Drug delivery

ABSTRACT

Chemodynamic therapy (CDT) has recently emerged as a promising treatment for cancer due to the high specificity of CDT towards tumor microenvironment (TME). However, the low efficiency of reactive oxygen species (ROS) generation and the robust ROS defensive mechanisms in cancer cells remain critical hurdles for current CDT. Addressing both challenges in a single platform, we developed a novel redox and light-responsive (RLR) nanoparticle with a core-shell structure. Remarkably, our hierarchical RLR nanoparticle is composed of an ultrasmall Fe₃O₄ nanoparticle engineered framework of hollow carbon matrix core and a nanoflower-like MnO₂ shell. Under the abundant overexpressed glutathione (GSH) and acidic nature in TME, the RLR nanoparticle was programmed to degrade and self-activate CDT-induced cancer-killing by accelerating ROS generation via overcoming the ROS defensive mechanisms based on the depletion of intracellular GSH, the sequential production of theranostic ion species (e.g., Mn²⁺ and Fe²⁺), a spatiotemporal controllable photothermal hyperthermia and a redox triggered chemotherapeutic drug release. Additionally, the carbon framework of RLR nanoparticle could collapse by leaching of iron ions. An excellent selective and near-complete tumor suppression based on the RLR nanoparticles through a strong synergy between CDT, PTT and anti-cancer drugs was demonstrated via *in vitro* and *in vivo* anti-tumoral assays.

1. Introduction

Reactive oxygen species (ROS) are a group of chemically reactive natural byproducts of the cell metabolism and encompass H₂O₂, superoxide (O₂⁻), and hydroxyl radical (·OH), which share crucial roles in cell signaling and homeostasis [1–3]. Recent interests in ROS-based cancer treatment have been driven by the breakthroughs on the understanding of critical pro-survival mechanisms in cancer and has shifted the paradigm of anti-tumor strategies [4–6]. Targeting multiple cancer survival pathways such as intracellular redox and immune surveillance has also been proven to be a more promising strategy to improve the outcome of chemotherapy or radiotherapy [5,7–10]. In this regard, chemodynamic therapy (CDT) has emerged as a promising alternative and supplements for conventional cancer treatment as it

produces ROS in a unique and tumor microenvironment (TME) specific manner [11–15]. More specifically, CDT catalyzes the conversion of less toxic H₂O₂ into more toxic ·OH with significantly higher oxidative potential typically via metal ion-mediated Fenton reaction to effectively induce ferroptotic pathways in cancer cells [5,16–19]. Due to the high concentrations of H₂O₂ in cancer cells, CDT is specific to TME, thereby minimizing side effects to healthy tissues compared to conventional photodynamic therapy [7,20–22]. Despite the clear advantages of CDT for cancer treatment, critical limitations remain in the low catalytic efficiency of H₂O₂ into ·OH conversion [23–26]. As such, the need for improving the catalytic efficiency of Fenton reaction and maximizing the toxic effects of ROS is clear in CDT-based cancer treatment [24].

Ferromagnetic nanoparticles have been mostly investigated to perform nanocatalase activity for CDT in a pH-dependent manner.

* Corresponding author.

** Corresponding author. Department of Chemistry and Chemical Biology, Rutgers University, Piscataway, NJ, 08854, USA.

E-mail addresses: qyzhang@nwpu.edu.cn (Q. Zhang), kblee@rutgers.edu (K.-B. Lee).

¹ These authors have contributed equally to this manuscript.

However, the relatively low release speed of ferrous ions under mild acidic tumor microenvironment significantly compromises the efficiency of CDT. Addressing this critical issue, ultrasmall Fe_3O_4 nanoparticles have shown great potential to accelerate the releasing of ferrous ions under mild acidic conditions but they often undergo fast clearance, leading to unsatisfactory pharmacodynamic profiles in CDT-based cancer treatment [25,27]. As such, it remains a major challenge on how to leverage ultrasmall Fe_3O_4 nanoparticles to accelerate ferrous ion release while maintaining a proper circulation rate. In addition to the slow releasing of iron ions, the efficiency of Fenton reaction has also been restricted by its intrinsically low catalytic efficiency as well as the limited H_2O_2 concentrations in cancer cells [23,25,28]. Toward this, one promising solution developed by scientists is to increase the temperature locally at the tumor site, which facilitates the Fenton reaction to overcome the activation barriers and increases $\cdot\text{OH}$ productivity. Moreover, recent reports indicate that certain hydroxyl radicals generated during the Fenton reaction can be scavenged by excess H_2O_2 , the temperature elevation-induced fast consumption of H_2O_2 could further counteract the detoxification of $\cdot\text{OH}$, thereby resulting in synergistic therapeutic effects between CDT and photothermal therapy (PTT) [24,29,30]. Nevertheless, conventional PTT reagents, such as noble metal nanomaterials, copper sulfides, carbon nanotubes and graphene, are typically non- or slow-biodegradable, thereby limiting their broad clinical applications [31]. Lastly, in addition to inefficient ROS production, unsatisfactory results from CDT-based cancer therapy has recently been attributed to ROS defensive mechanisms adapted by cancer [32]. For example, the elevation of ROS levels is heavily associated in the early stage of cancer development [33,34]. In response to such elevated ROS levels, cancer adapts stronger ROS defensive systems including higher glutathione (GSH) levels [13,32,35,36]. Therefore, it remains critical hurdles to simultaneously overcome the ROS defensive mechanism in cancer cells and achieve high efficiency for ROS generation in CDT-based cancer treatment.

To this end, we developed a novel redox and light-responsive (RLR) nanoparticle-based platform for synergistic induction of ROS sequentially through GSH depletion, Fenton reaction, photothermal hyperthermia and chemotherapy (Fig. 1a). We rationally designed our RLR nanoparticle platform with a hierarchical core-shell hybrid structure; the core is composed of ultrasmall iron oxide nanoparticles (Fe_3O_4) embedded in an amorphous hollow carbon framework ($\text{Fe}_3\text{O}_4\text{-C}$), and the shell is composed of MnO_2 nanosheet stacked flower-like structures (Fig. 1b). When the core-shell nanoparticle entered the cancer cell, the high level of GSH in cancer cells would degrade the MnO_2 shell and lead to simultaneous depletion of GSH, releasing magnetic resonance imaging (MRI) contrast agent Mn^{2+} , and exposing the inner Fe_3O_4 core to the cancer cytoplasm. Due to the high acidity of cancer cytoplasm, the ultrasmall Fe_3O_4 nanoparticles released iron ions (Fe^{2+} and Fe^{3+}) sequentially, which could self-activate the Fenton reaction by catalyzing the conversion of H_2O_2 into more toxic $\cdot\text{OH}$ radicals (Fig. 1c) [18]. In this process, without any external stimulation, the RLR nanoparticle could activate CDT by reducing intracellular antioxidant GSH and sequential generating $\cdot\text{OH}$. Meanwhile, the carbon framework with high absorption in the near-infrared (NIR) region enabled “light-responsive” property to generate controllable hyperthermia to accelerate the ROS generation via enhancing the catalytic efficiency intracellularly (Fig. 1c) [12]. Afterward, the core-shell nanoparticles were fully degraded with the etching of iron oxide nanoparticles and the dissociation of carbon framework into a cleavable form, thereby providing a safe nanotherapeutic platform for *in vivo* and clinical applications. To maximize the cancer-killing efficiency, we further combined and loaded doxorubicin (DOX), a clinically used anti-cancer drug that not only block topoisomerase II but also generate ROS (H_2O_2) to further amplify the outcome of CDT through the catalysis of the nicotinamide adenine dinucleotide (phosphate) (NAD(P)H), to the core-shell nanoparticle and then delivered into the cancer cell in a target-specific manner (Fig. 1c) [37,38]. *In vitro* drug uptake assay also

revealed an interesting photothermal (PTT)-enhanced accumulation and therapeutic effect of anti-cancer drugs to amplify the combinatorial therapy between CDT and chemotherapy (Fig. 1d). Taking advantage of the synergy among CDT, photothermal hyperthermia, and anti-cancer drug delivery in a single platform, we successfully achieved cancer-killing efficiency of 99.4% and 99% *in vitro* and *in vivo*, respectively (Fig. 1e). These results collectively indicated the potential of RLR nanoparticles-based platform for the efficient clinical tumor treatment and imaging.

2. Materials and methods

2.1. Chemicals and reagents

Ferrocene, acetone, carbamide, potassium permanganate, methylene blue trihydrate (MB), 2', 7'-dichlorodihydrofluorescein diacetate (DCFH-DA), Doxorubicin (DOX), hydrogen peroxide (H_2O_2) and reduced glutathione (GSH) were purchased from Sigma-Aldrich Co. (St Louis, MO, USA). Calcein-AM and PI were bought from Invitrogen (USA). PBS (pH 7.4), fetal bovine serum (FBS), DMEM, RPMI, trypsin-EDTA and penicillin-streptomycin were purchased from Gibco Co., Ltd. (Carlsbad, CA, USA). All chemical agents were of analytical grade and were used directly with no further purification.

2.2. Synthesis of $\text{Fe}_3\text{O}_4\text{-C}$ nanoparticles and RLR nanoparticles

The $\text{Fe}_3\text{O}_4\text{-C}$ hollow nanoparticles were synthesized by a novel one-step hydrothermal method. In a typical synthesis, ferrocene (3.00 g) and carbamide (0.80 g) were dissolved in acetone (300 mL). After intense sonication for 30 min, 30 mL of 30% H_2O_2 solution was slowly added into the above solution, which was vigorously stirred for 30 min with magnetic stirring apparatus. The precursor solution was transferred into a 500.0 mL Teflon-lined stainless-steel autoclave. After sealing, the autoclave was heated to and maintained at 200 °C for 24 h. The autoclave was cooled naturally to room temperature. After intense sonication for 15 min, the products from the Teflon-lined stainless-steel autoclave was magnetized for 10 min by a magnet of 0.20 T. The supernatant was discarded under a magnetic field. The precipitates were washed with acetone and DI water three times respectively. Finally, the black products were dried via lyophilization.

The synthesis of RLR nanoparticles was based on the redox reaction. Firstly, 50 mg of $\text{Fe}_3\text{O}_4\text{-C}$ nanoparticles were dispersed in 10 mL of 1 mM KMnO_4 aqueous solution. The solution was heated to 80 °C for 1 h under stirring. The products were purified by DI water for three times. The as-obtained nanoparticles were dried via lyophilization.

2.3. Surface modification with iRGD

To modify with targeting modality iRGD, the water-soluble RLR nanoparticles from above were first diluted with DPBS to reach a final concentration of 2 mg mL⁻¹. Afterward, excess 10 kDa branched PEI (Sigma-Aldrich) was added dropwise (1 mg mL⁻¹) and spun overnight. After that, the PEI-coated RLR nanoparticles were mixed with heterobifunctional linker Sulfo-SMCC (0.1 mM) and incubated at room temperature for 4 h with continuous shaking. Simultaneously, SH-PEG-COOH moieties were linked to iRGD-NH₂ moieties using EDC/NHS coupling. After that, thiolated PEG-iRGD constructs were added to the thiol-reactive Sulfo-SMCC-linked RLR-PEI complexes. The resulting mixture was allowed to react overnight, followed by purification by DI water three times.

2.4. Drug loading and release

The $\text{Fe}_3\text{O}_4\text{-C}$ and RLR nanoparticles were dispersed in an aqueous solution of DOX with a final concentration of 1 mg mL⁻¹. The solution was stirred overnight for DOX loading. Purification was performed

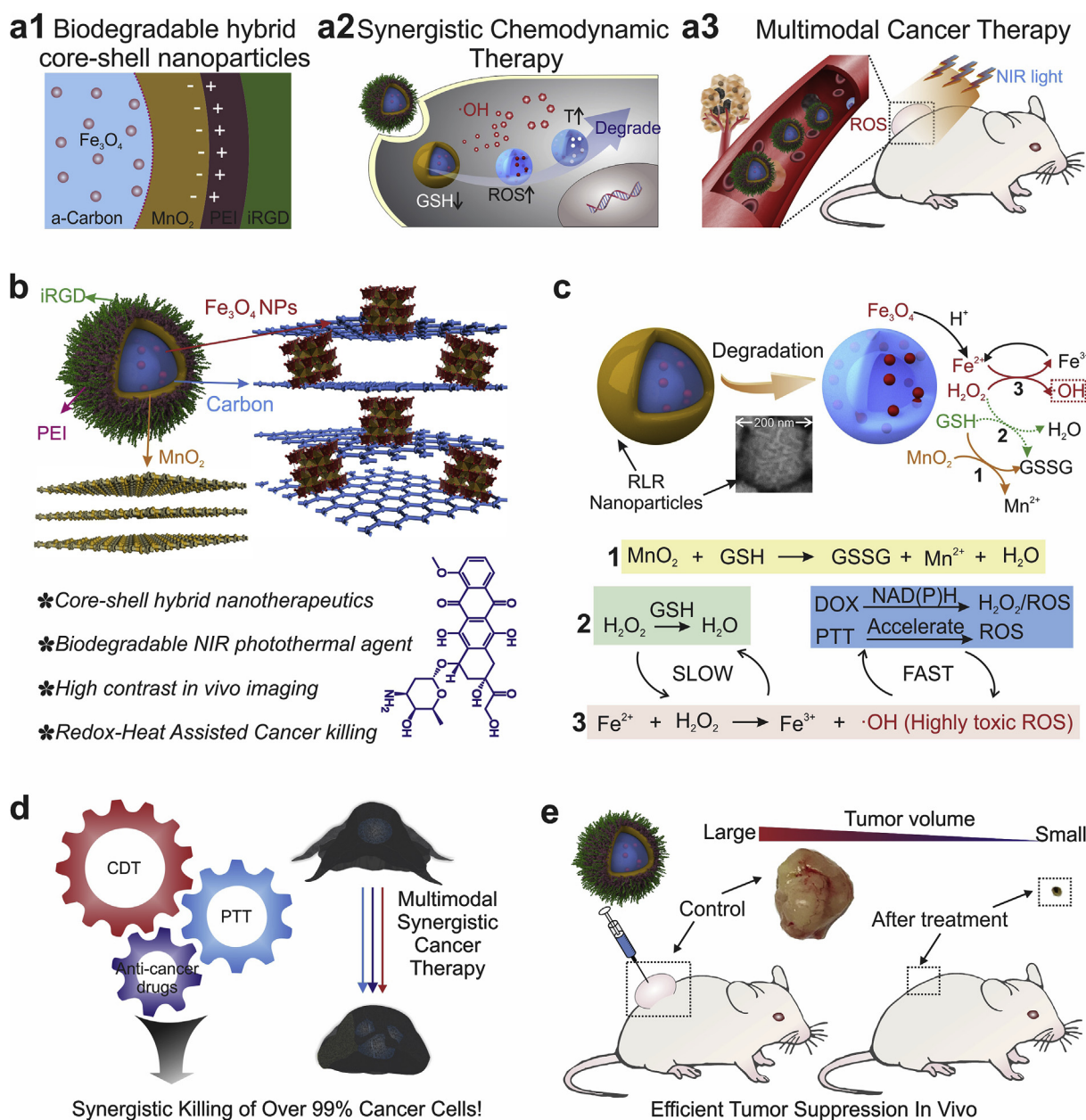


Fig. 1. Schematic diagram illustrating the photothermal and RLR nanoparticle-enhanced chemodynamic therapy (CDT) for synergistic cancer therapy. **a1**, Schematic diagrams showing the development of redox and light-responsive (RLR) nanoparticles. **a2**, this unique nanostructure overcomes the two critical barriers for CDT by accelerating reactive oxygen species (ROS) generation through photothermal (PTT) hyperthermia and depleting glutathione (GSH). **a3**, a diagram illustrating the RLR nanoparticle-based efficient and selective *in vivo* cancer therapy through programmed CDT, PTT hyperthermia and delivery of anti-cancer drugs. **b**, A 3D illustration of **a1** showing the unique composition and structure of RLR nanoparticles and their distinctive advantages for the multimodal cancer therapy. The inset chemical structure in a dark-blue color represents the anti-cancer drug (DOX) used in this study. **c**, Mechanisms on the synergistic effects for the CDT based on the GSH reduction by MnO_2 , Fenton reaction by iron ions and the temperature increase by photothermal hyperthermia. **d-e**, Multimodal cancer therapy for *in vitro* cancer apoptosis (**d**) and *in vivo* tumor suppression (**e**) based on the synergy between CDT, PTT and the targeted delivery of drugs. (For interpretation of the references to color in this figure legend, the reader is referred to the Web version of this article.)

twice, then the DOX-loaded Fe_3O_4 -C nanoparticles (Fe_3O_4 -C-DOX) and RLR nanoparticles (RLR-DOX) were dispersed in Dulbecco's Phosphate Buffered Saline (DPBS). The loading weight percentage of DOX in the final amounts of the nanoparticle (20 mg) was calculated based on the following equation:

$$\text{DOX (\%)} = \frac{(C_b - C_a) \text{ mg/mL} \times 2 \text{ mL}}{20 \text{ mg} + [(C_b - C_a) \text{ mg/mL} \times 2 \text{ mL}]}$$

where C_b and C_a represent the weight concentration (mg/mL) before (C_b) and after (C_a) incubation with nanoparticles [39].

The Redox-triggered DOX release kinetics were further conducted.

Two concentration groups of GSH were used. For each group, RLR-DOX nanoparticles (20 mg) were incubated in 20 mL GSH solution (2 μM or 10 mM) under stirring. At different time points, a portion of the solution (1 mL) was collected for centrifugation. The absorption of the supernatant was measured by a UV-Visible spectrometer (Varian Cary 50 spectrophotometer, CA) using maximum absorption of DOX at 480 nm. The DOX content in the solution was determined by a standard curve.

2.5. Degradation kinetics

Degradation of the RLR nanoparticles (200 $\mu\text{g mL}^{-1}$) was evaluated

by mimicking intracellular GSH concentration (GSH, 10 mM) in pH = 5.0 (dibasic sodium phosphate-citric acid) buffer under constant rotation. At predetermined time points (2 h, 4 h, 6 h, 8 h, 1 day, 2 days, 5 days, 7 days, 9 days), samples were collected for TEM, UV-vis-NIR adsorption, DLS, and the Fe^{2+} , Mn^{2+} concentrations were measured by ICP-MS to quantitatively evaluate the degradation kinetics.

2.6. Photothermal performance of $\text{Fe}_3\text{O}_4\text{-C}$ and RLR nanoparticles

Photothermal performance of $\text{Fe}_3\text{O}_4\text{-C}$ and RLR nanoparticles was assessed by 808 nm laser irradiation with various power densities in a 96-well culture plate containing 100 μL $\text{Fe}_3\text{O}_4\text{-C}$ or RLR nanoparticles dispersion (PBS, pH = 7.4) with varying concentrations. The temperature of the irradiated aqueous dispersion was recorded by a thermal probe.

2.7. The intracellular concentration of GSH detection

MDA-MB-231 cells were seeded in a six-well plate (10×10^5 per well) and cultured to be fully confluent [32]. After treatment with varied concentration of RLR nanoparticles for 6 h at 37 °C, cells were harvested, washed with PBS and lysed on ice in 40 μL of Triton-X-100 lysis buffer. After 1 h, lysates were centrifuged at 9800 g and 200 μL of the supernatant was mixed with 1000 μL of Ellman's reagent (0.5 mM DTNB). The amount of GSH was quantified by measuring the absorbance at 405 nm using a UV-vis-NIR spectrophotometer. Percentage of GSH content from treated cells were compared with untreated cells.

2.8. The $\cdot\text{OH}$ generation, detection and the promotive effect of heat

Study of the $\cdot\text{OH}$ generation was conducted by analyzing the degradation of methylene blue (MB) as reported previously [24]. In brief, the absorbance at 644 nm of MB solution ($50 \mu\text{g mL}^{-1}$) with or without 400 μM of H_2O_2 was measured before or after the addition of Fe^{2+} (100 μM). Electron paramagnetic resonance (EPR) spectroscopy was then employed to further ensure the generation of $\cdot\text{OH}$ and the ability of heat-enhanced hydroxyl radical yield accurately using 5,5-Dimethyl-1-pyrroline N-oxide (DMPO) as a spin trapping agent for $\cdot\text{OH}$. With 80 μL of DMPO buffer solution (100 mM) in a dark EP tube, the subsequent reaction groups included the following additions respectively: 1) 40 μL H_2O_2 (1 mM) + 20 μL 10 $\mu\text{g mL}^{-1}$ RLR nanoparticles at pH = 7.4; 2) 40 μL H_2O_2 (1 mM) + 20 μL 10 $\mu\text{g mL}^{-1}$ RLR nanoparticles at pH = 5.0; 3) 40 μL H_2O_2 (1 mM) + 20 μL 10 $\mu\text{g mL}^{-1}$ RLR nanoparticles at pH = 5.0 with 5 min heating using 320 K water for several seconds. Immediately, the mixture was transferred into a quartz capillary using capillarity, X-band EPR spectra were then measured at room temperature in perpendicular mode on a Bruker EMX-8/2.7 spectrometer and recorded with the following settings: microwave frequency = 9.872 GHz, microwave power = 6.375 mW, modulation frequency = 100.00 kHz and modulation amplitude = 1.00 G.

2.9. Intracellular ROS detection

MDA-MB-231 cells were seeded in 24-well plates at an amount of 2×10^4 for 24 h and incubated with the following additions respectively: i) cells without any treatment; ii) cells incubated with Fe_3O_4 ; iii) cells incubated with MnO_2 ; iv) cells incubated with RLR for another 24 h. After incubation with 1 mL DCFH-DA (10 μM in FBS-free DMEM) at 37 °C in 5% CO_2 for 20 min, cells were washed with PBS three times. The level of intracellular ROS was evaluated by detecting the fluorescence of DCF ($\lambda_{\text{ex}} = 488 \text{ nm}$, $\lambda_{\text{em}} = 525 \text{ nm}$) with a fluorescence microscope [25]. We calculate the intracellular ROS based on the population of ROS signal detected cells.

2.10. In vitro studies

Cytotoxicity of the samples was evaluated under various concentrations. human dermal fibroblasts (HDFs), adipose-derived stem cells (ADSCs), C2C12 cells, MDA-MB-231 cells, Hela cells, and DU-145 cells were seeded on 96 well plates at an initial density of 1.0×10^4 cells per well and incubated overnight. A solution of free DOX, RLR nanoparticles, RLR-NIR (808 nm, 1.5 W cm^{-2} , 5 min, FC-808-5W, CNI laser, Changchun, China), RLR-DOX, RLR-DOX-NIR (808 nm, 1.5 W cm^{-2} , 5 min) at various concentrations were incubated with cells for further 48 h. After incubation, cells were washed with DPBS and medium was replaced by 100 μL of Prestoblue solution containing medium. After incubation for 30 min, the fluorescence at 590 nm (excited at 560 nm) was measured by a microplate reader.

The half maximal inhibitory concentration (IC_{50}) was conducted under various DOX concentrations (0.1, 0.5, 1.0, 5.0, 10, 20, 30, 50 μM) and pretreated with fresh medium (control), RLR nanoparticles ($50 \mu\text{g mL}^{-1}$), and RLR nanoparticles under laser irradiation ($50 \mu\text{g mL}^{-1}$, 808 nm, 1.5 W cm^{-2} , 5 min) and incubated for another 24 and 48 h.

2.11. In vivo anti-cancer efficacy

All animal work was conducted following the regulation of the Institutional Animal Care and Use Committee (IACUC) at Rutgers University.

To develop the breast tumor xenograft mouse model, MDA-MB-231 (5.0×10^6) cells were mixed with Matrigel (BD Biosciences, San Jose, CA) and were transplanted to the flanks of mice via subcutaneous injection. For *in vivo* therapeutic evaluation, mice were randomly assigned ($n = 3$) into three groups. In particular, tumors were generated on both sides of the flanks in the experimental group mice. The anti-cancer experiments were performed until the volume of tumors reached 100 mm^3 . Three groups for different treatments contained the following conditions: group 1) 50 μL per site of PBS as a control; group 2) 50 μL per site of DOX (28 μM); group 3) 50 μL per site of DOX-loaded RLR nanoparticles (with a concentration of $300 \mu\text{g mL}^{-1}$). To confirm the photothermal therapeutic efficacy, 808 nm laser was irradiated (5 min, 1.5 W cm^{-2}) to the right side of tumors while left side tumors were not irradiated. Using a digital caliper to monitor the volume of the tumors every 3–4 days lasting 28 days after the corresponding experiments. The tumor volumes were calculated according to the following equation: $V = \text{length} \times \text{width} \times \text{height} \times 3.14 \times 6^{-1}$. The normalized tumor volume was defined as $V_{\text{R}} = V \times V_0^{-1} \times 100\%$. The body weights were measured every 3–4 day to evaluate the *in vivo* toxicity.

The pathological tissue sections of the tumor and major organs (*i.e.* heart, liver, spleen, kidney, and lung) were collected for hematoxylin and eosin (H&E) staining assay. The terminal deoxynucleotidyl transferase dUTP nick end labeling (TUNEL) analysis was performed on the tumor slides.

The fresh tumors were washed with PBS and transferred into liquid nitrogen for *in vivo* PCR analysis. After crushing, the total RNA was isolated using TRIzol Reagent and analyzed as previously mentioned [39].

2.12. In vitro and in vivo MR imaging

The magnetic resonance (MR) imaging was conducted under anesthesia on a 3T MRI scanner with the following parameters: field of view = $5 \times 3 \text{ cm}^2$ matrix size = 384×256 , slice thickness = 1 mm, echo time (TE) = 8 ms, and repetition time (TR) = 300 ms, 500 ms, 1000 ms, 2000 ms. The Mn concentration of RLR nanoparticle in aqueous solution was determined by ICP-MS. To test the MR imaging performance, different concentrations of RLR nanoparticles were incubated with 10 mM GSH for 20 min, and the supernatant was collected and placed in Eppendorf tubes (2 mL volume) for MRI scanning. T1

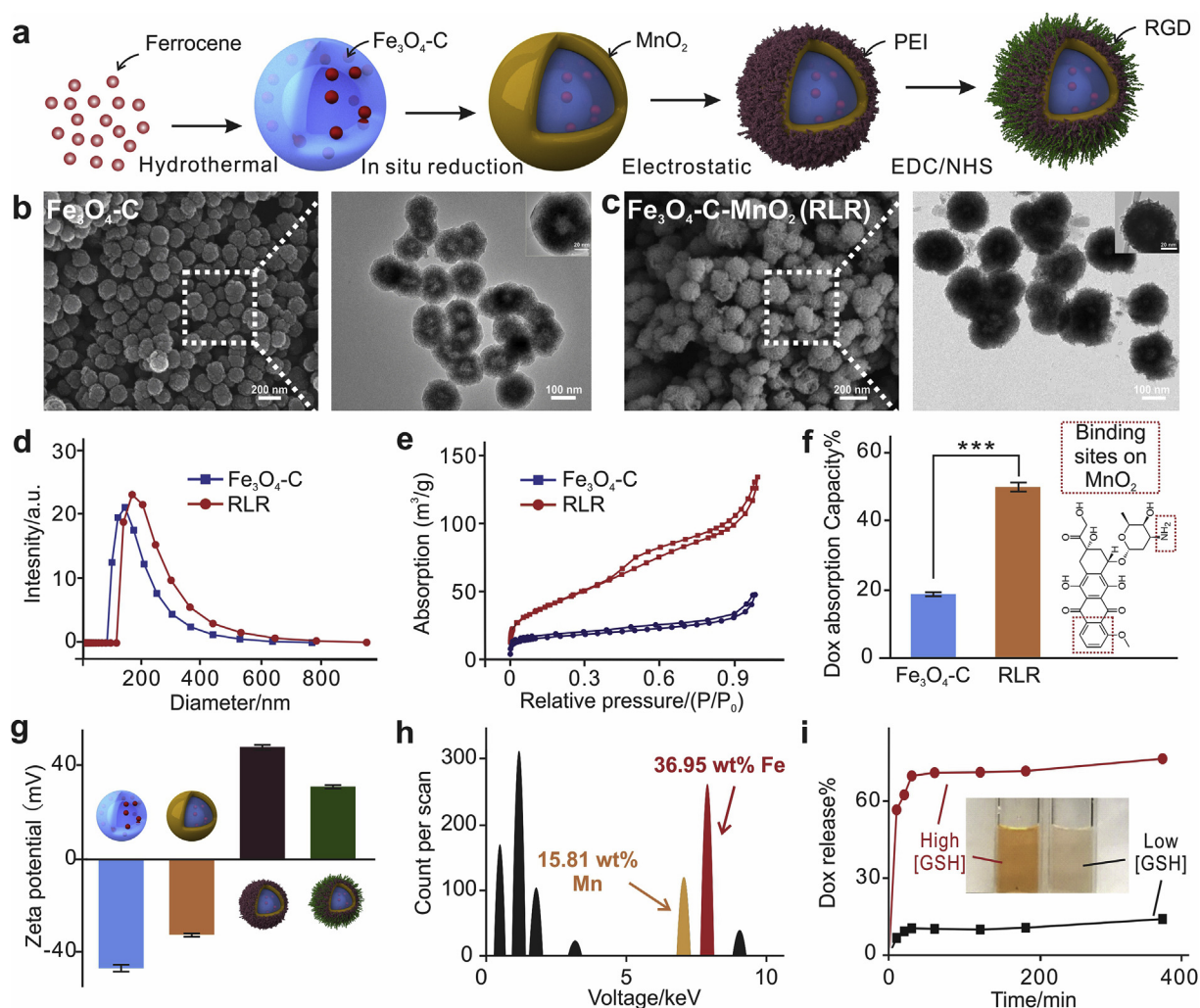


Fig. 2. Synthesis and characterization of redox and light responsive nanoparticles for enhanced CDT. **a**, Schematic diagram illustrating the synthesis of RLR nanoparticles with a core shell hybrid structure through two reactions. **b-c**, Representative SEM (left) and TEM (right) images showing the hollow structure of $\text{Fe}_3\text{O}_4\text{-C}$ (**b**) and the additional layer of MnO_2 with the nanosheets-stacked structure of RLR nanoparticles (**c**). **d**, Hydrodynamic size distributions of the $\text{Fe}_3\text{O}_4\text{-C}$ and RLR nanoparticles. **e-f**, Gas adsorption properties characterized by the Brunauer-Emmett-Teller measurement showing significantly increased surface area of the RLR nanoparticles compared to $\text{Fe}_3\text{O}_4\text{-C}$ nanoparticles (**e**), which further leads to better loading capacities of RLR nanoparticles towards clinically used anti-cancer drugs, as shown in the drug loading assay using UV-Vis absorption spectrum at a wavelength of 480 nm (**f**, inset image: the chemical formulation of doxorubicin). **g**, Zeta potential measurements characterizing the step-by-step construction of RLR nanoparticles as shown in panel **a**. **h-i**, Energy diffraction spectroscopy (EDS), **h**) confirmed the stimuli (GSH)-triggered degradation of RLR nanoparticles by using the EDS bands of Mn and Fe; Drug (DOX) release curve from RLR nanoparticles was monitored by the colorimetric measurement (**i**).

value was measured on a GE workstation (ADW4.6) (GE Healthcare, Milwaukee, Wisc., USA). For *in vivo* MR imaging, RLR nanoparticles were injected and monitored its performance after 0, 1, 2, 3, 5, 24, and 96 h, respectively.

3. Results and discussion

3.1. Synthesis of RLR nanoparticles for anticancer drug loading and delivery

The success of our synergistic multimodal cancer therapy was built up upon a wide spectrum of unique material properties, which included: i) the manipulation of redox-based depletion of GSH and Fenton reactions for CDT; ii) high conversion efficiency of NIR light to thermal energies for PTT; iii) tumor targeting and homing capabilities; and iv) a robust biodegradability for safe nanomedicine. Based on these considerations, we designed the hybrid nanostructure with the $\text{Fe}_3\text{O}_4\text{-C}$ as the core with the MnO_2 nanoshell. Starting from molecular precursors, two sequential redox reactions synthesized our hierarchical

multifunctional RLR nanoparticle with the desired compositions and sizes organized in a core-shell structure (Fig. 2a-d, Figs. S1-2). The small size of Fe_3O_4 nanoparticles (2 nm) facilitated the leaching of $\text{Fe}^{2+}/\text{Fe}^{3+}$ under acidic conditions, essential for the induction of Fenton reaction [18]. On the other hand, the carbon matrix, not only provided NIR absorption and photothermal hyperthermia but also acted as a template for synthesizing the MnO_2 nanoshell. More specifically, a second redox reaction between the carbon (reductant) and KMnO_4 (oxidant) initiated the *in situ* growth of MnO_2 nanoshell onto the core nanoparticles, as reflected by the changes of hydrodynamic sizes and transmission electron microscope (TEM) images (Fig. 2c-d, Figs. S3-4). The MnO_2 nanoshell was then utilized for intracellular redox manipulation by receiving electrons from GSH and simultaneously enhancing drug loading content (49.8%) through the increased surface area ($162\text{ m}^2\text{ g}^{-1}$) and the non-covalent interactions between MnO_2 and the anti-cancer drug DOX (Fig. 2e and f). The high drug loading capacity further improved anticancer activity and reduced cytotoxicity. These two critical properties laid down the fundamentals for improved CDT and chemotherapy. As demonstrated, the additional coating of a

disulfide-based cyclic arginine glycine aspartic peptide (iRGD) could further enable active targeting towards tumor *in vivo* and is achieved through the electrostatic assembly with polyethyleneimine (PEI) followed by amidization (Fig. 2a, g) [39,40]. In parallel, increasing demands on safe nanomedicine in clinical applications would require the nanotherapeutics to be biodegradable and cleared from the human body timely to avoid chronic inflammation [41–43]. In this regard, the RLR nanoparticles could undergo sequential degradation of MnO₂ shell and Fe₃O₄-C core in response to the high GSH levels and acidic cytoplasm in the tumor, thereby meeting the standard for clinical applications (Fig. 2h). Equally importantly, the TME-specific degradation of RLR nanoparticles brought additional modalities to selectively target and eliminate cancer cells when the nanoparticles were loaded with anti-cancer drugs. As a result of the TME-specific degradation of the RLR nanoparticle, release profile of anti-cancer drugs was much faster (5.46-fold increase) at high GSH concentration (10 μM, which represented the TME) compared to the control condition (2 μM, representing the extracellular microenvironment) (Fig. 2i). Overall, considering the significant disparity of GSH concentration between physiological conditions and cancer cells, the distinctive stimuli-responsive drug release suggests a good potential of RLR-based platform for delivering clinically used anti-cancer drugs with minimal side effects from passive diffusion of drugs.

3.2. RLR nanoparticles-based redox regulation in cancer cells

Cancer cells overproduce ROS during the initial stage of tumor growth and typically develop stronger ROS defensive mechanisms with high concentrations of GSH [5,32,44]. In this regard, our hybrid RLR nanoparticles undergoing step-wise biodegradation to reduce GSH levels and simultaneously produce theranostic ion species (e.g., Mn²⁺ and Fe²⁺) for enhanced CDT (Fig. 3a and b). Specifically, after entering cancer cells through endocytosis, the MnO₂ shell on RLR nanoparticles reacted with intracellular GSH to yield Mn²⁺ and glutathione disulfide (GSSH) (Fig. 3c–e). Consistent with previous reports [13], the addition of RLR nanoparticles, which contained MnO₂ as a shell, directly led to a concentration-dependent decrease of GSH level signals in the Ellman's assay, (Fig. 3f and g). After the dissolution of the outer shell, the iron oxide nanoparticles in the core would degrade to produce iron ions due to combined effects from GSH and the high acidity of cancer cytoplasm [24,45]. Lastly, the degradation of iron oxide destabilized the carbon framework, leading to the dissociation of carbon into small graphitic segments (less than 5 nm on average), which could be excreted by the human body (Figs. S5–6) [46]. During these sequential reactions, the released Fe²⁺/Fe³⁺ worked as catalysts for Fenton reaction. Therefore, RLR nanoparticles amplified the oxidative stress by reducing GSH and transforming the less toxic form of ROS (H₂O₂) into a more lethal form (e.g., ·OH) (Fig. S7) [5,13,47]. To test the ROS generation from the RLR nanoparticles, we treated metastatic breast cancer cells (MDA-MB-231) with the particles and three control groups were included: MnO₂ nanoshell alone; Fe₃O₄-C core alone; and no treatment group. The RLR nanoparticles treated cells showed significantly higher signal (85.3%) of intracellular ROS compared to the control (18.5%, no treatment) (Fig. 3h). Most importantly, when the RLR nanoparticles delivered to the cancer cells, the ROS levels are much higher even compared to the group with GSH reduction (by MnO₂) alone and the Fenton reaction (by Fe₃O₄-C) alone, strongly suggesting a synergistic mechanism between these two critical ROS generation pathways of Fe²⁺ generation and GSH depletion, which is consistent with previous reports on ferroptotic pathways [13]. Moreover, we further treated MDA-MB-231 cells with varying concentrations of RLR nanoparticle under mild acid condition (pH = 6.5) that mimic the tumor microenvironment (Fig. S8). The cell variability could be dramatically reduced (23.1%) compare to normal condition (79.5%) under the concentration of 100 μg mL⁻¹, which indicated acid could accelerate the Fenton reaction induced by iron oxide nanoparticles and enhance the therapeutic effect via ferroptosis

pathway. Given their high potency for synergistic induction of oxidative stress, RLR nanoparticles could serve as excellent CDT reagents for cancer therapy.

3.3. Photothermal hyperthermia-enhanced chemodynamic therapy

In addition to the effective delivery of CDT modalities, RLR nanoparticles also provided orthogonal modalities of photothermal hyperthermia to improve the catalytic efficiency of CDT by elevating the local temperature. The spatiotemporally controllable photothermal hyperthermia was achieved by using an 808 nm NIR laser for its deeper tissue penetration property *in vivo* (Fig. 4a) [31,48–52]. Due to the existence of carbon matrix in the Fe₃O₄-C core, which strongly absorbs 808 nm NIR light, our core-shell RLR nanoparticles showed “light-responsive” property to convert light into heat under the 808 nm laser [53–55]. For example, even under a low laser power density of 1.5 W cm⁻², we identified a significant temperature (15 °C) increase within 5 min towards mild hyperthermia (Fig. 4b and c). As a control, water under identical irradiation conditions did not show any noticeable heating effect. Based on these results, we calculated the photothermal conversion efficiency of RLR nanoparticles to be 26.8%, which is comparable to the most efficient NIR photothermal reagents such as graphene (Fig. S9) [56]. While water bath-based hyperthermia has also been clinically used for sensitizing cancer towards apoptosis [57], the RLR nanoparticles-based NIR photothermal hyperthermia penetrates deeper tissues with high efficiencies and can be better controlled spatiotemporally, which is much beneficial to minimize side effects on surrounding healthy tissues and better serves our therapeutic purposes in multimodal therapy [31].

Instead of sensitizing cancer towards apoptosis, PTT could also speed up the formation of lethal ·OH in CDT by directly amplifying the catalytic effects of iron ions [12,23,24]. We delivered RLR nanoparticles to the cancer cells, irradiated cells with NIR and compared the ROS generation to the control group (RLR nanoparticle without NIR) to verify the effects of PTT on ROS generation. By performing live-cell ROS assay, a significantly higher level of ROS (23.9% increase) showed up in the laser exposed experimental group compared to the control experiment (RLP nanoparticle delivery alone) (Fig. 4d). This result directly testified to the PTT-enhanced ROS generation, critical for enhancing the anti-cancer outcome in CDT. Additionally, by performing the measurements under a higher temperature (45 °C, experimental condition), we mimicked the NIR hyperthermia *in vitro*. Electron paramagnetic resonance (EPR) was further used to detect ·OH *in situ*, and we directly confirmed the enhanced production of ROS originated from the accelerated Fenton reaction under the acidic conditions (Fig. 4e) [5,24]. Our results indicated the heat generated from photothermal hyperthermia could robustly accelerate and improve RLR nanoparticles-based CDT via ferroptosis pathways on a single platform.

3.4. Anti-cancer drug accumulation induced by NIR photothermal hyperthermia

RLR nanoparticles not only provide efficient PTT for improving CDT but also deliver clinically used chemotherapeutic drugs in a single platform for cancer-killing. Interestingly, we confirmed that RLR nanoparticles-based PTT could also enhance the accumulation of chemotherapeutic agent in cancer cells to facilitate chemotherapy (Fig. 4f). In the clinical settings, several cancer cells (e.g., breast cancer cells) often become resistant towards anti-cancer drugs after repeated chemotherapy, which is known as the process of chemoresistance [39]. While mechanisms remain largely unclear, the increased drug efflux associated with ATP-binding cassette (ABC) transporter families and inhibited apoptosis have been identified as the critical pathways for chemoresistance [58]. In this regard, hyperthermia can be a promising solution [53,59–61]. For example, the temperature increase can effectively modulate the metabolism in cancer cells, downregulate drug

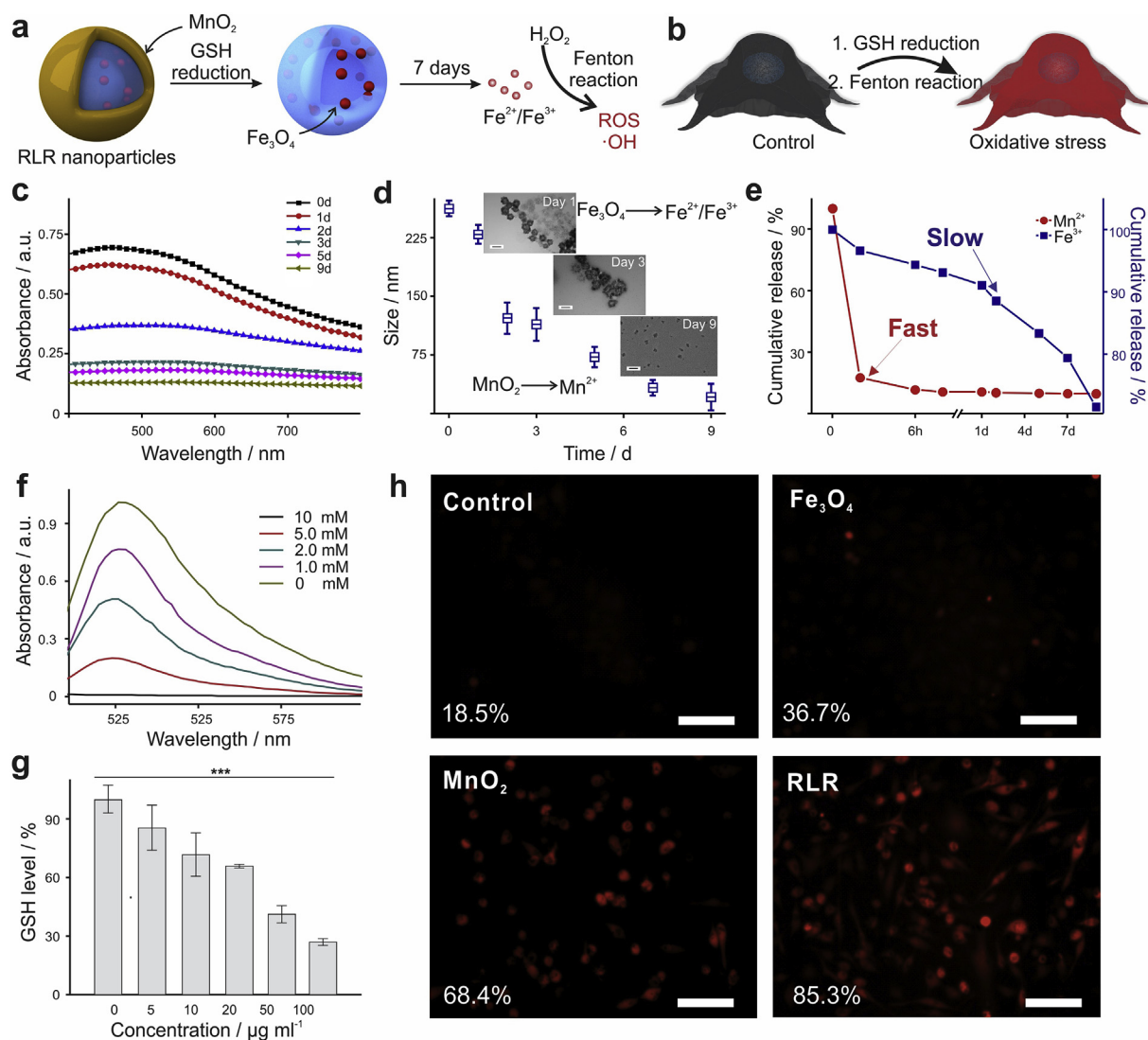


Fig. 3. Synergistic induction of CDT by combined GSH depletion and Fenton reaction mediated by RLR nanoparticles. **a-b**, Schematic diagrams illustrating the mechanism of synergistic CDT. The red color indicates the oxidative stress from the ROS generation. **c-e**, The degradation of RLR nanoparticles and the sequential production of Mn^{2+} and iron ions for the synergistic CDT, which are characterized by the time-dependent colorimetric reduction of the RLR nanoparticles in the UV-Vis absorption spectrum (**c**), the time-dependent size decreases of RLR nanoparticles in the transmission electron microscopy (TEM) (**d**) and the elemental composition of the degraded RLR nanoparticles in the Inductively Coupled Plasma-Mass Spectrum (ICP-MS, **e**). **f**, The inhibitory effect of various concentration of GSH on ROS (using 10 mM H_2O_2 as exemplary ROS modality) was investigated by detecting the fluorescence spectrum of DCF. **g**, Constant decrease of the GSH levels during the addition of RLR nanoparticles, which is characterized by a colorimetric GSH sensor (Ellman's reagent DNTB). **h**, An intracellular ROS generation assay comparing four different compositions validated the synergy between MnO_2 -based GSH depletion and iron ions-based Fenton reaction for the CDT. The red pseudocolor indicates the production of ROS intracellularly. Scale bars: 100 μm . Error bar represent mean \pm s.d.; $n = 4$, *** $p < 0.001$. (For interpretation of the references to color in this figure legend, the reader is referred to the Web version of this article.)

efflux pathways, DNA repair, and mitochondrial turbulence, and thereby increase drug accumulation, cell apoptosis and partially overcome the chemoresistance [62,63]. To verify the effects of NIR photothermal hyperthermia on drug uptake, we initiated photothermal hyperthermia using optimized conditions (1.5 W cm^{-2} , 5 min) and performed anti-cancer drug uptake assay using MDA-MB-231 cancer cells. Based on the fluorescent intensity of DOX in cell cytoplasm, a significantly (1.93-fold) increased drug accumulation was found intracellularly in the experimental condition compared to the no-treatment control group (Fig. 4g). Such drug accumulation continued to rise in a time-dependent manner throughout a 24 h process (Fig. 4h). These results strongly indicate the successful increase of drug uptake and reduced drug efflux in cancer cells mediated by RLR nanoparticles. We further analyzed the change of gene expression pattern that is related to drug efflux to investigate the mechanisms behind the enhanced drug

accumulation (Fig. 4i, Table S1). From the qRT-PCR experiments, we reliably identified an upregulation of Heat shock factor 1 (HSF-1 genes: 3.45-fold), a downregulation of drug efflux gene MDR-1 (2.81-fold) and antiapoptosis gene TP53 (3.52-fold) in the photothermal treated group compared to the control, which is consistent with our drug uptake assay and directly proves the NIR-irradiated RLR nanoparticles can target the drug-resistant pathways [59]. In parallel, a significant downregulation on the proapoptotic genes (BCL-2, 4.31-fold), and upregulation of proapoptotic genes (BAX, 4.29-fold and Caspase 3, 3.77-fold) confirmed the ability of RLR nanoparticle to sensitize cancer cells towards proapoptotic status resulting from drug accumulation (Fig. S10). Moreover, since DOX can generate H_2O_2 through the catalysis of the NAD(P)H, the accumulated DOX shows great promise for tumor-specific H_2O_2 level amplification [37]. In order to prove that, MDA-MB-231 cancer cells were incubated with DOX with different concentrations for 2 h and the

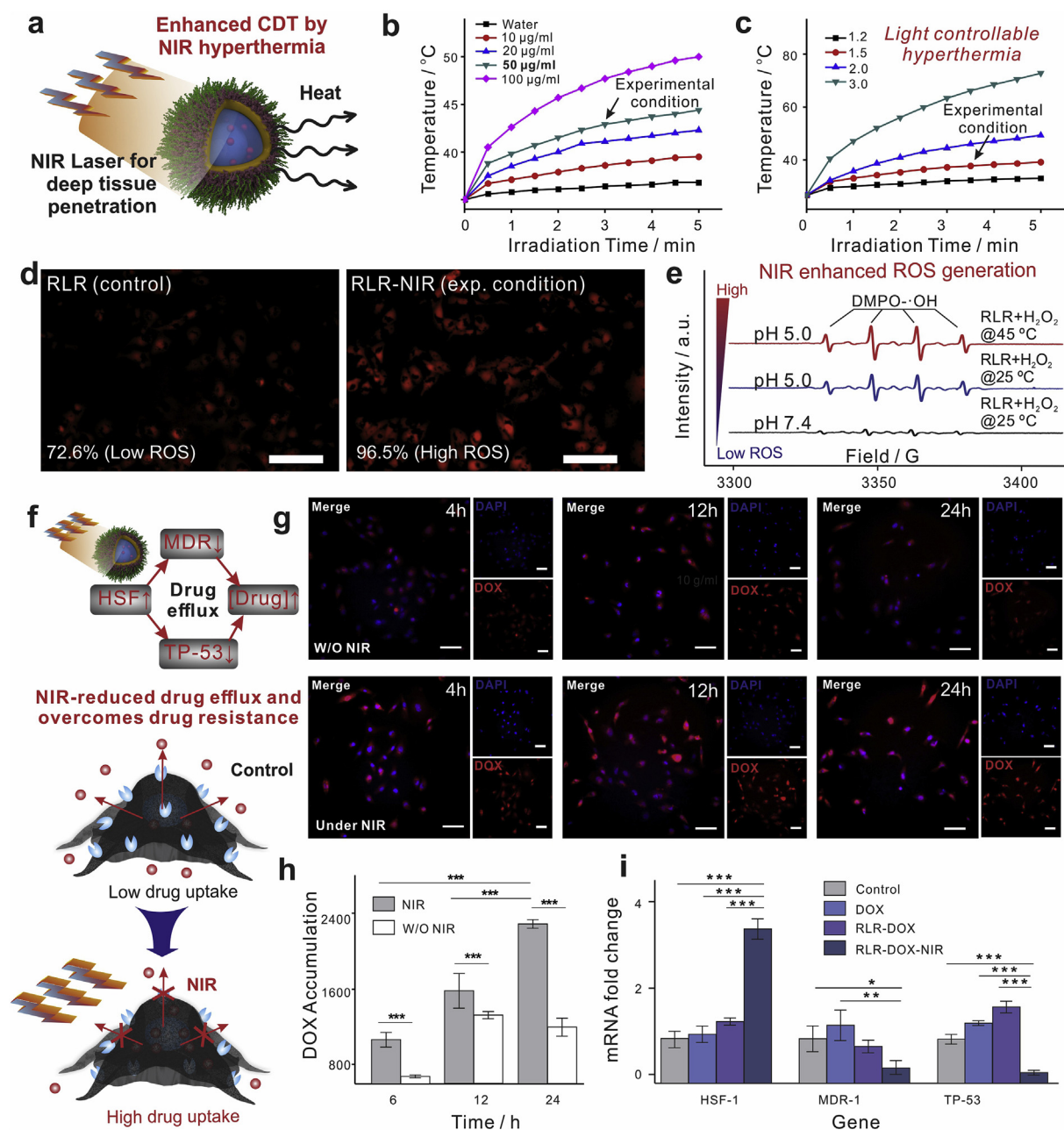


Fig. 4. Enhancing CDT and drug accumulation in cancer cells by RLR-induced NIR photothermal hyperthermia for synergistic anti-cancer therapy. **a-c**, Schematic illustration of localized photothermal effect under 808 nm NIR laser irradiation. **b-c**, Temperature of the NIR-induced photothermal hyperthermia can be facilely controlled by either the concentration of RLR nanoparticles (**b**) or the power intensity of NIR lasers (**c**). **d**, The contribution of NIR photothermal hyperthermia to the CDT can be validated in an intracellular ROS detection. Intracellular ROS production is indicated by the red color. **e**, by accelerating the reaction rates of Fenton reaction, NIR photothermal hyperthermia increased the generation of highly toxic ROS $\cdot\text{OH}$ by using Electron Paramagnetic Resonance (EPR) measurement. **f**, Schematic diagram showing the RLR nanoparticles-based NIR photothermal hyperthermia can sensitize the cancer cells towards multimodal anti-cancer therapy by reducing the drug efflux in chemoresistant cancer cells. **g-h**, The NIR photothermal hyperthermia induced reduction of drug efflux and enhanced accumulation of drugs were confirmed by a time-dependent drug uptake assay. Red color in the fluorescent images represents the fluorescence from the model drug (doxorubicin, DOX). **i**, The mechanism of photothermal hyperthermia-mediated reduction of drug efflux is validated in a qRT-PCR experiment based on the significant suppression of MDR-1 and TP-53 pathways in the NIR treated experimental group compared to the treatment of nanoparticle alone. Error bar represent mean \pm s.d.; j: n = 10, k: n = 4, ***p < 0.001, **p < 0.01, *p < 0.05. (For interpretation of the references to color in this figure legend, the reader is referred to the Web version of this article.)

generated H_2O_2 was stained with a ROS probe, 2',7'-dichlorofluorescein diacetate (DCFH-DA). Dichlorofluorescein (DCF), the oxidized product of DCFH-DA, showed increased fluorescence in cancer cells with higher concentration of DOX, indicating more H_2O_2 was generated (Fig. S11). Collectively, the combination of heating stress and anti-cancer drugs provide unique modalities to synergistically sensitize the cancer cells to death by utilizing RLR nanoparticles.

3.5. RLR nanoparticles-based synergistic cancer killing in vitro

Our goal is to develop the RLR nanoparticle-based multimodal therapy for the synergistic killing of cancer via synergies among CDT, PTT and chemotherapy. Through the CDT, the RLR nanoparticles directly target the ferroptosis pathways of cancer cells. By NIR irradiation, PTT further enhances CDT, overcome drug-resistant pathways,

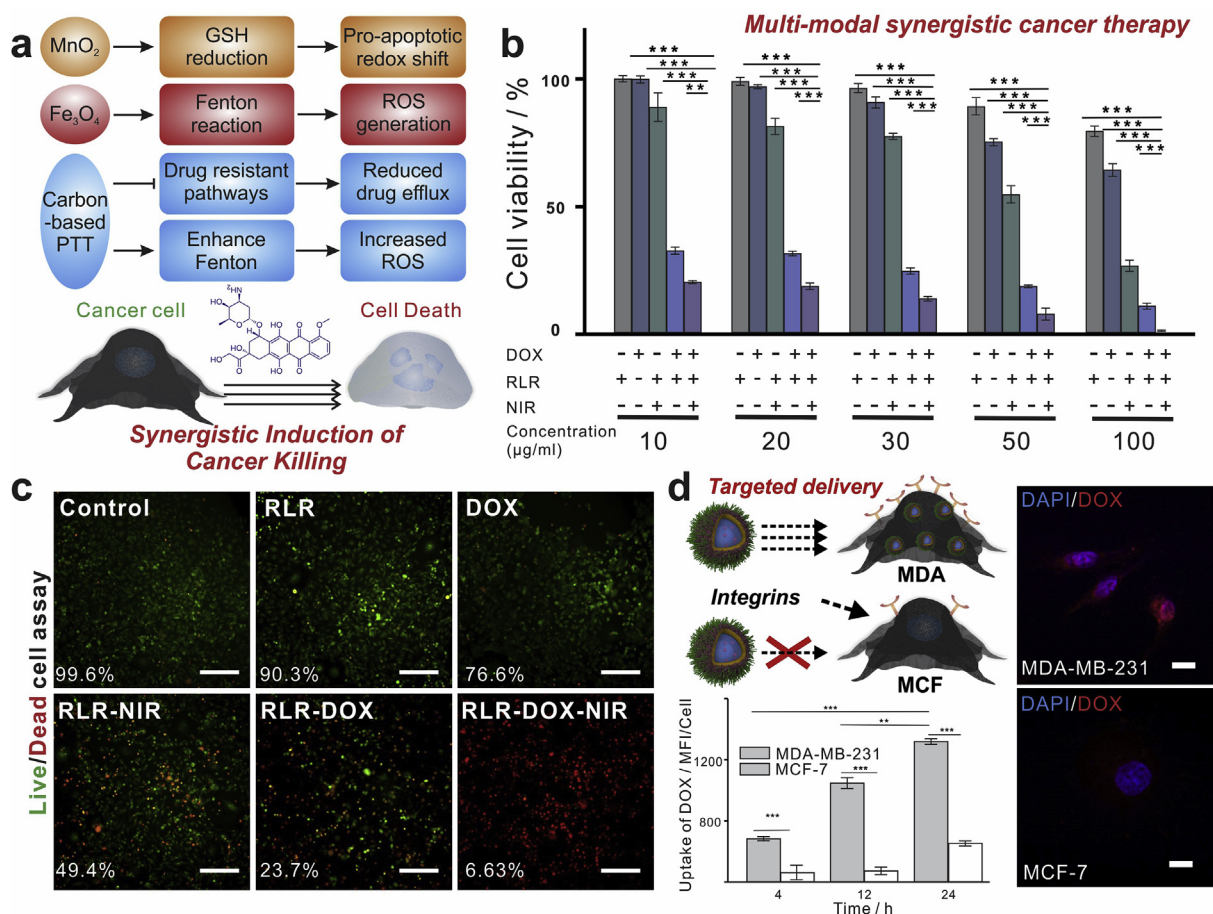


Fig. 5. The synergistic anti-cancer effects mediated by RLR nanoparticles-based CDT and photo-chemical effects. **a**, Illustrations showing the mechanism for the synergistic induction of cancer death by combined CDT, PTT and delivery of anti-cancer drugs on a single platform. **b-c**, The synergistic killing of cancer cells confirmed in an *in vitro* cell apoptotic assay (**b**) and live-dead staining (**c**) on the experimental group (RLR nanoparticles combined with PTT and delivery of anti-cancer drugs) and control groups. Percentage of live cells were listed in the bottom left corner of each fluorescent image in **c**. Scale bars in **c**: 100 µm. **d**, Targeted delivery of RLR nanoparticles and anti-cancer drugs (DOX) to the malignant cell (MDA-MB-231), which is achieved by the surface coating of iRGD on RLR nanoparticles. The two fluorescent images represent the differential uptake of nanoparticles in malignant cancer cells (top) and control cells (bottom) based on the red fluorescence from the DOX delivered by the nanoparticle. The bottom left graph summarizes the statistical information of a time-dependent accumulation of nanoparticles in the two different cancer cells. Scale bars: 10 µm. Error bar represent mean ± s.d.; **b**: n = 3, **d**: n = 10, ***p < 0.001, **p < 0.01. (For interpretation of the references to color in this figure legend, the reader is referred to the Web version of this article.)

and simultaneously shift cancer towards pro-apoptotic status. Combining these strategies in a single platform, the RLR nanoparticles can significantly improve the potency of clinically used anti-cancer drugs (Fig. 5a). To test the therapeutic outcome from the drug-loaded RLR nanoparticles, we first performed a comprehensive cancer apoptosis assay *in vitro* by delivering DOX-loaded RLR nanoparticles at varying concentrations followed by NIR treatment (RLR-NIR-DOX). As controls, four additional groups were included: i) RLR nanoparticles alone; ii) DOX alone; iii) RLR nanoparticles with NIR (RLR-NIR), and iv) DOX-loaded RLR nanoparticles without NIR (RLR-DOX). From the results of cancer apoptosis assay, RLR nanoparticles exhibited good biocompatibility towards normal cells (Fig. S12). While RLR-NIR and RLR-DOX groups induced significant apoptosis of three types of cancer cells at all concentrations in a clear dosage-dependent manner (Fig. 5b, Fig. S13, Table S2). Remarkably, by combining the NIR treatment and the DOX treatment, we lowered IC₅₀ of DOX to 0.38 µM (80 times decrease compared to the DOX-only group) (Fig. S14). The synergistic effects from multimodality of cancer therapy tested in a live-dead cell assay showed a consistent trend as discovered from the cell apoptosis assay, further validating the unique cancer-killing mechanisms (Fig. 5c). Moreover, we further calculated the synergy index among CDT, PTT and chemotherapy to be well above 1.02, further suggesting a synergistic effect between the multimodal therapy. We also modified the

RLR nanoparticles with iRGD to augment tumor targeting-abilities of the highly potent therapeutic platform (Fig. S15). More specifically, the iRGD peptide binds to α_vβ₃ integrin, which is overexpressed in many cancer cells (e.g., metastatic breast cancer cells) [40,64]. By delivering the iRGD-modified and DOX-loaded RLR nanoparticles into a control breast cancer cell line (MCF-7 cells, low integrin expression cell line), we demonstrated the targeted specific delivery based on a significantly higher (2-fold increase) fluorescence (Fig. 5d) and selective killing of malignant cancer cells (MDA-MB-231). These results indicated not only successful conjugation of functional iRGD to the particle but also the suitability of this targeting strategy for specific targeting.

3.6. RLR nanoparticles-based *in vivo* cancer therapy

Following the promising *in vitro* findings, we further applied our RLR nanoparticles for *in vivo* imaging and tumor suppression (Fig. 6a). To be consistent with the *in vitro* experiments, we used a breast cancer model to show the efficacy of RLR nanoparticles as a proof-of-concept. We identified the demonstration of targeted delivery of RLR nanoparticles to the tumor sites and the subsequent degradation *in vivo* as the primary interest before performing tumor suppression assay. As such, we first conducted an *in vivo* nanoparticle distribution assay by establishing a tumor model with MDA-MB-231 cells via subcutaneous

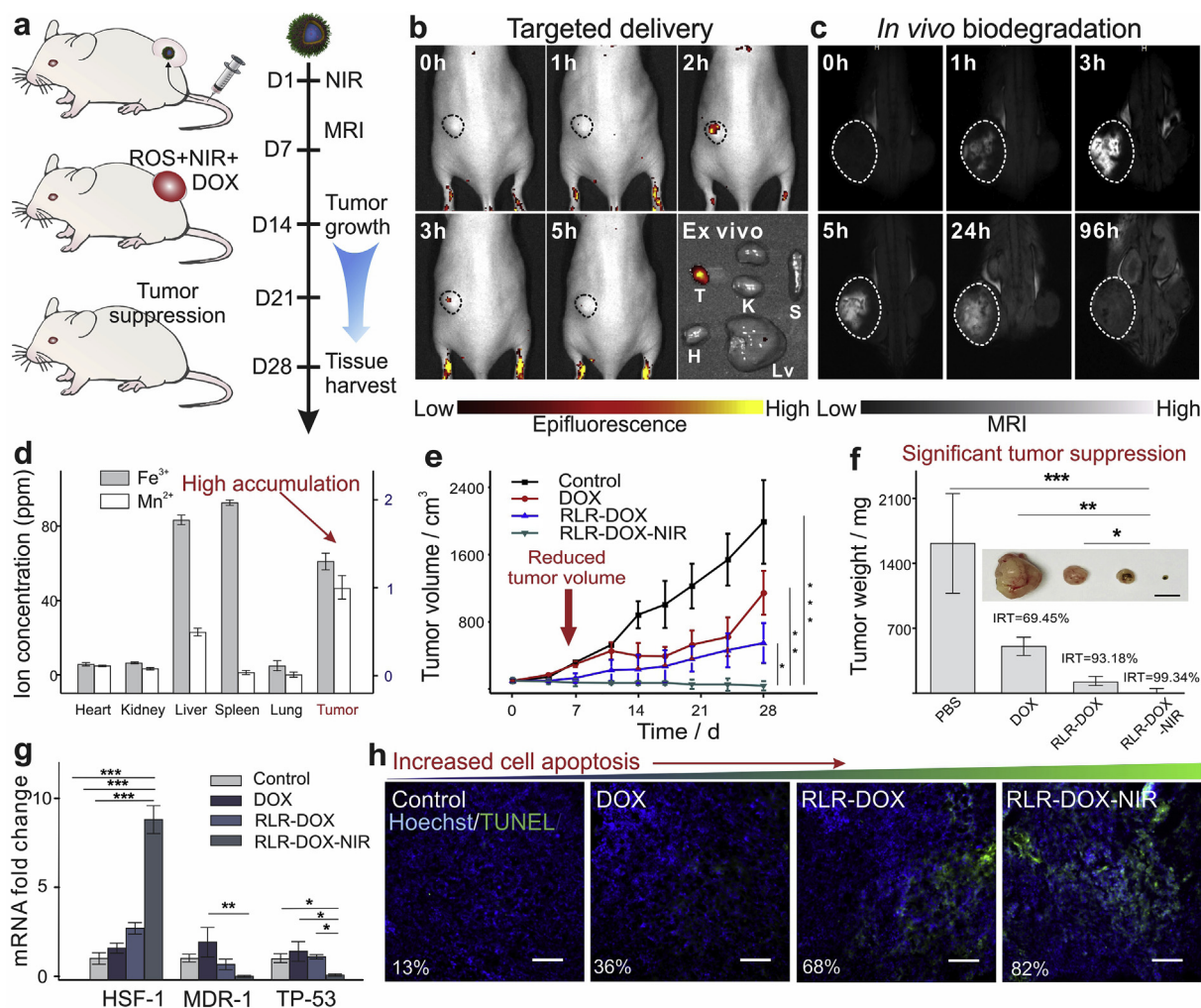


Fig. 6. Complete suppression of tumor growth *in vivo* based on the RLR nanoparticles and NIR photothermal mediated CDT. **a**, Schematic diagram illustrating the injection process and timeline of the multimodal cancer therapy and MR imaging after the treatment of RLR nanoparticles. **b-c**, Time-dependent *in vivo* biodistribution assay (**b**) and MR imaging (**c**) illustrating the targeted delivery of RLR nanoparticles to the tumor sites and the biodegradation *in vivo* and *ex vivo* based on the MRI active Mn^{2+} ions. T: Tumor, H: Heart, K: Kidney, Lv: Liver, and S: Spleen. **d**, The biodistribution of RLR nanoparticles were further validated by the organ-differential elemental distributions through ICP-MS. **e**, Synergistic tumor suppression by RLR nanoparticles validated by tracking *in vivo* tumor sizes. **f**, Over 99% of tumor growth was suppressed by the experimental group (RLR-DOX-NIR) compared to the PBS-treated group. Insert shows the representative image of each testing group (PBS, DOX, RLR-DOX, and RLR-DOX-NIR, respectively). Scale bar: 1 cm **g**, Mechanisms for the synergistic killing of cancer cells through the multimodal therapy revealed by *in vivo* gene expression in a qRT-PCR experiment. **h**, TUNNEL assay staining the DNA damage further reveals the significantly higher apoptosis in the tumor site of the experimental condition comparing to the control groups. Scale bars: 100 μm . Error bar represent mean \pm s.d.; **e**, **f**: $n = 3$, **g**: $n = 4$, $***p < 0.001$, $**p < 0.01$, $*p < 0.05$.

injection to the mice. After the tumor formation, the FITC labeled-RLR nanoparticles were intravenously injected through the tail vein. The targeted delivery of RLR nanoparticles to the tumor site was successfully confirmed by the significant *in vivo* fluorescence signal at the tumor after 2 h, suggesting a minimal side effect caused by a non-specific delivery to the healthy organs (Fig. 6b). Such fast accumulation would also be helpful for achieving a stronger cytotoxic effects on cancer cells and is consistent with other nanoparticle-based delivery platforms that combine both active and negative targeting [65,66]. In parallel, we utilized MR imaging for validating biodistribution assay and confirmed the biodegradation profile of the RLR nanoparticles, and T_1 relaxation rate with GSH treatment was up to $5.11 \text{ mM}^{-1} \text{ s}^{-1}$ (Fig. 6c, Fig. S16). The images solidly demonstrated the TME responsive MRI performance of RLR nanoparticle. The high value of r_1 also reflected the RLR nanoparticle could be a good candidate for further diagnosis applications. The *in situ* MR imaging capability of RLR nanoparticles was enabled by the release of T_1 MRI positive probes (Mn^{2+}) from the RLR nanoparticles when degraded by the cancer cells. From

the *in situ* MRI results, we found that while the initial nanoparticles injection did not yield noticeable MRI signals, a constant increase of MRI intensities was observed throughout the time course between 1 h and 3 h. Thereafter, MRI intensity plateaued between 5 and 24 h followed by a signal decrease until 96 h after injection (Fig. S17). These results indicated that the RLR nanoparticles accumulated selectively and degraded timely *in vivo* at the tumor sites, which were among the critical considerations for clinical applications. Additionally, according to our previous results, the onset of T_1 MRI signals quantitatively correlated with the drug release profile as the RLR nanoparticles degraded; therefore, through MRI, we were able to give quantitative measurements of drug release *in vivo* in a tumor model [67].

Furthermore, the RLR nanoparticles-based platform showed superior anti-cancer outcome *in vivo* as well. Although many nanoparticle-based therapeutic approaches have been developed for cancer treatment, our strategy was advantageous for clinical applications being selective to tumor redox microenvironment, spatiotemporal controllable, and provided high cancer-killing efficacy through synergistic

effects from CDT, PTT, and chemotherapy. By creating a xenograft mouse tumor model using the identical method [39], we first validated the assay based on the exponential increase of tumor volume and the suppression of tumor growth (1.74-fold) from chemotherapy (DOX alone) (Fig. 6e). As a result of CDT and chemotherapy, the delivery of chemotherapeutics by RLR nanoparticles slowed down tumor growth significantly by 3.63-fold compared to the no treatment group. Most importantly, mice treated by the experimental condition, which was the combined CDT, PTT, and chemotherapy almost stopped the tumor growth completely throughout the 1-month observation, directly supporting our findings *in vitro* and the strong synergies using the multimodal cancer therapy. In the experimental condition, the NIR-triggered PTT not only improved the outcome of ROS generation in CDT but also increased drug accumulation and apoptotic pathways to enhance the efficacy of chemotherapy, thereby leading to the synergistic effect. Moreover, due to the relatively low power density we used for PTT, no skin burn was found on the mice, which indicated that localized mild PTT did not cause obvious side effect (Fig. S18). We found a similar trend in tumor weights harvested from different groups of animals, with a dramatic higher decrease for the experimental group compared to all the controls (Fig. 6f). Moreover, additional gene analysis from the dissected tumor tissue also revealed the suppression of drug efflux related genes (HSF-1, MDR-1, and TP-53) and the upregulation of pro-apoptotic genes (BAX and Caspase 3) (Fig. 6g, Fig. S19, Table S1). As a result, the experimental condition showed a significantly higher percentage of DNA damage and apoptosis in the TUNEL assay and H&E staining compared to the control (Fig. 6h, Fig. S20). Also, this treatment did not induce any significant change of the bodyweight as well as toxicity in the histological analysis of major organ section (Figs. S21–22). While more mechanistic investigations would be essential to elucidate the interactions between the RLR nanoparticles-based CDT and PTT modalities *in vivo*, our results strongly supported the potential of RLR nanoparticle-based therapeutic platform for robust tumor suppression.

4. Conclusions

In summary, as a proof of concept, we developed a multifunctional nanoparticle-based versatile platform as synergetic CDT-PTT-Chemo therapeutics for the treatment of cancer. A novel hierarchical RLR nanoparticle composed of the core-shell structure was successfully synthesized and characterized with excellent drug loading and redox-triggered releasing, high photothermal conversion efficiency and programmed biodegradability. Most importantly, the RLR nanoparticle advances current CDT-based cancer treatment first by enduing a self-activated ROS generation via stepwise GSH depletion and Fenton reaction, and then by accelerating the lethal radical formation through spatiotemporally controlled hyperthermia (PTT). Furthermore, based on the RLR nanoparticle-enabled CDT, we rationally designed an advanced combinatorial cancer therapy with PTT and a clinically used chemotherapy and successfully achieved near-complete killing of cancer cells *in vitro* and *in vivo*. Comprehensive gene analysis revealed the PTT and CDT improve the outcome of clinically used anti-cancer drugs by reducing drug efflux and downregulating cancer pro-survival pathways, respectively. To the best of our knowledge, this is the first study to construct activatable theranostic nanosystem for MRI-monitored CDT-PTT-Chemo combinatorial cancer therapy.

Given the versatility of our synthetic routes for the core-shell nanoparticles, our work can inspire more investigations on hierarchical nanoparticles with programmable biodegradability for next-generation safe nanomedicine. Also, considering their high clinical relevance, our single platform-based delivery of CDT, PTT and chemotherapy with thorough mechanistic studies opens a new avenue towards highly efficient anti-tumoral nanomedicine with high versatility and minimal toxicity. Currently, we are working on the evaluation of the developed therapeutic platform for treating drug-resistant and more lethal (e.g.,

pancreatic cancer) tumor models by further engineering its hierarchical nanostructures and delivering cancer-specific epigenetic drugs.

Conflicts of interest

The authors declare no competing financial interest.

Acknowledgments

S.W. and L. Y. contributed equally to this work. Q.Z. acknowledge partial financial support from the State Key Program of National Natural Science of China (Grand No. 51433008) and the Fundamental Research Funds for the Central Universities (Grand No. 3102017jc01001). K.B.L. acknowledges the financial support from the New Jersey Commission on Spinal Cord (CSCR17IRG010; CSCR16ERG019).

Appendix A. Supplementary data

Supplementary data to this article can be found online at <https://doi.org/10.1016/j.biomaterials.2019.119498>.

References

- [1] E. Piskounova, M. Agathocleous, M.M. Murphy, Z. Hu, S.E. Huddleston, Z. Zhao, A.M. Leitch, T.M. Johnson, R.J. DeBerardinis, S.J. Morrison, Oxidative stress inhibits distant metastasis by human melanoma cells, *Nature* 527 (7577) (2015) 186–191.
- [2] D. Trachootham, J. Alexandre, P. Huang, Targeting cancer cells by ROS-mediated mechanisms: a radical therapeutic approach? *Nat. Rev. Drug Discov.* 8 (7) (2009) 579–591.
- [3] B. D'Autreaux, M.B. Toledano, ROS as signalling molecules: mechanisms that generate specificity in ROS homeostasis, *Nat. Rev. Mol. Cell Biol.* 8 (10) (2007) 813–824.
- [4] L. Raj, T. Ide, A.U. Gurkar, M. Foley, M. Schenone, X. Li, N.J. Tolliday, T.R. Golub, S.A. Carr, A.F. Shamji, A.M. Stern, A. Mandinova, S.L. Schreiber, S.W. Lee, Selective killing of cancer cells by a small molecule targeting the stress response to ROS, *Nature* 475 (7355) (2011) 231–234.
- [5] H. Wang, Z. Gao, X. Liu, P. Agarwal, S. Zhao, D.W. Conroy, G. Ji, J. Yu, C.P. Jaroniec, Z. Liu, X. Lu, X. Li, X. He, Targeted production of reactive oxygen species in mitochondria to overcome cancer drug resistance, *Nat. Commun.* 9 (1) (2018) 562.
- [6] H.Y. Cho, A. Mavi, S.D. Chueng, T. Pongkulapa, N. Pasquale, H. Rabie, J. Han, J.H. Kim, T.H. Kim, J.W. Choi, K.B. Lee, Tumor homing reactive oxygen species nanoparticle for enhanced cancer therapy, *ACS Appl. Mater. Interfaces* 11 (2019) 23909–23918.
- [7] C. Holohan, S. Van Schaeybroeck, D.B. Longley, P.G. Johnston, Cancer drug resistance: an evolving paradigm, *Nat. Rev. Cancer* 13 (10) (2013) 714–726.
- [8] W. Fan, W. Bu, B. Shen, Q. He, Z. Cui, Y. Liu, X. Zheng, K. Zhao, J. Shi, Intelligent MnO₂ nanosheets anchored with upconversion nanoprobes for concurrent pH-/H₂O₂-responsive UCL imaging and oxygen-elevated synergetic therapy, *Adv. Mater.* 27 (28) (2015) 4155–4161.
- [9] S.C. Formenti, S. Demaria, Combining radiotherapy and cancer immunotherapy: a paradigm shift, *J. Natl. Cancer Inst.* 105 (4) (2013) 256–265.
- [10] H. Lin, Y. Chen, J. Shi, Nanoparticle-triggered in situ catalytic chemical reactions for tumour-specific therapy, *Chem. Soc. Rev.* 47 (6) (2018) 1938–1958.
- [11] H. Ranji-Burachaloo, P.A. Gurr, D.E. Dunstan, G.G. Qiao, Cancer treatment through nanoparticle-facilitated Fenton reaction, *ACS Nano* 12 (12) (2018) 11819–11837.
- [12] Z. Tang, Y. Liu, M. He, W. Bu, Chemodynamic therapy: tumour microenvironment-mediated Fenton and fenton-like reactions, *Angew. Chem. Int. Ed. Engl.* 58 (4) (2019) 946–956.
- [13] S. Wang, F. Li, R. Qiao, X. Hu, H. Liao, L. Chen, J. Wu, W. Haibin, M. Zhao, J. Liu, R. Chen, X. Ma, D. Kim, J. Sun, T.P. Davis, C. Chen, J. Tian, T. Hyeon, D. Ling, Arginine-rich manganese silicate nanobubbles as a ferroptosis-inducing agent for tumor-targeted theranostics, *ACS Nano* 12 (12) (2018) 12380–12392.
- [14] W. Ke, J. Li, F. Mohammed, Y. Wang, K. Tou, X. Liu, P. Wen, H. Kinoh, Y. Anraku, H. Chen, K. Kataoka, Z. Ge, Therapeutic polymersome nanoreactors with tumor-specific activable cascade reactions for cooperative cancer therapy, *ACS Nano* 13 (2) (2019) 2357–2369.
- [15] L. Zhang, S.S. Wan, C.X. Li, L. Xu, H. Cheng, X.Z. Zhang, An adenosine triphosphate-responsive autocatalytic Fenton nanoparticle for tumor ablation with self-supplied H₂O₂ and acceleration of Fe(III)/Fe(II) conversion, *Nano Lett.* 18 (12) (2018) 7609–7618.
- [16] S.J. Dixon, K.M. Lemberg, M.R. Lamprecht, R. Skouta, E.M. Zaitsev, C.E. Gleason, D.N. Patel, A.J. Bauer, A.M. Cantley, W.S. Yang, B. Morrison 3rd, B.R. Stockwell, Ferroptosis: an iron-dependent form of nonapoptotic cell death, *Cell* 149 (5) (2012) 1060–1072.
- [17] B.R. Stockwell, J.P. Friedmann Angeli, H. Bayir, A.I. Bush, M. Conrad, S.J. Dixon, S. Fulda, S. Gascon, S.K. Hatzios, V.E. Kagan, K. Noel, X. Jiang, A. Linkermann, M.E. Murphy, M. Overholtzer, A. Oyagi, G.C. Pagnussat, J. Park, Q. Ran, C.S. Rosenfeld, K. Salnikow, D. Tang, F.M. Torti, S.V. Torti, S. Toyokuni,

- K.A. Woerpel, D.D. Zhang, Ferroptosis: a regulated cell death nexus linking metabolism, redox biology, and disease, *Cell* 171 (2) (2017) 273–285.
- [18] S.E. Kim, L. Zhang, K. Ma, M. Riegman, F. Chen, I. Ingold, M. Conrad, M.Z. Turker, M. Gao, X. Jiang, S. Monette, M. Pauliah, M. Gonen, P. Zanzonico, T. Quinn, U. Wiesner, M.S. Bradbury, M. Overholzer, Ultrasmall nanoparticles induce ferroptosis in nutrient-deprived cancer cells and suppress tumour growth, *Nat. Nanotechnol.* 11 (11) (2016) 977–985.
- [19] W. Zhang, S. Li, X. Liu, C. Yang, N. Hu, L. Dou, B. Zhao, Q. Zhang, Y. Suo, J. Wang, Oxygen-generating MnO₂ nanodots-anchored versatile nanoplatform for combined chemo-photodynamic therapy in hypoxic cancer, *Adv. Funct. Mater.* 28 (13) (2018) 1706375.
- [20] Q. Chen, C. Liang, X. Sun, J. Chen, Z. Yang, H. Zhao, L. Feng, Z. Liu, H₂O₂-responsive liposomal nanoprobe for photoacoustic inflammation imaging and tumor theranostics via in vivo chromogenic assay, *Proc. Natl. Acad. Sci. U. S. A.* 114 (21) (2017) 201701976.
- [21] T.P. Szatrowski, C.F. Nathan, Production of large amounts of hydrogen peroxide by human tumor cells, *Cancer Res.* 51 (3) (1991) 794–798.
- [22] J. Ge, M. Lan, B. Zhou, W. Liu, L. Guo, H. Wang, Q. Jia, G. Niu, X. Huang, H. Zhou, X. Meng, P. Wang, C.S. Lee, W. Zhang, X. Han, A graphene quantum dot photodynamic therapy agent with high singlet oxygen generation, *Nat. Commun.* 5 (2014) 4596.
- [23] W. Feng, X. Han, R. Wang, X. Gao, P. Hu, W. Yue, Y. Chen, J. Shi, Nanocatalysts-augmented and photothermal-enhanced tumor-specific sequential nanocatalytic therapy in both NIR-I and NIR-II biowindows, *Adv. Mater.* 31 (5) (2019) e1805919.
- [24] Z. Tang, H. Zhang, Y. Liu, D. Ni, H. Zhang, J. Zhang, Z. Yao, M. He, J. Shi, W. Bu, Antiferromagnetic pyrite as the tumor microenvironment-mediated nanoplatform for self-enhanced tumor imaging and therapy, *Adv. Mater.* 29 (47) (2017) 1701683.
- [25] M. Huo, L. Wang, Y. Chen, J. Shi, Tumor-selective catalytic nanomedicine by nanocatalyst delivery, *Nat. Commun.* 8 (2017) 357.
- [26] L. Wang, M. Huo, Y. Chen, J. Shi, Iron-engineered mesoporous silica nanocatalyst with biodegradable and catalytic framework for tumor-specific therapy, *Biomaterials* 163 (2018) 1–13.
- [27] L. Gao, J. Zhuang, L. Nie, J. Zhang, Y. Zhang, N. Gu, T. Wang, J. Feng, D. Yang, S. Perrett, X. Yan, Intrinsic peroxidase-like activity of ferromagnetic nanoparticles, *Nat. Nanotechnol.* 2 (9) (2007) 577–583.
- [28] W.P. Li, C.H. Su, Y.C. Chang, Y.J. Lin, C.S. Yeh, Ultrasound-induced reactive oxygen species mediated therapy and imaging using a Fenton reaction activable polymer-some, *ACS Nano* 10 (2) (2016) 2017–2027.
- [29] Z. Tang, P. Zhao, D. Ni, Y. Liu, M. Zhang, H. Wang, H. Zhang, H. Gao, Z. Yao, W. Bu, Pyroelectric nanoplatform for NIR-II-triggered photothermal therapy with simultaneous pyroelectric dynamic therapy, *Mater. Horizon.* 5 (5) (2018) 946–952.
- [30] P. Hu, T. Wu, W. Fan, L. Chen, Y. Liu, D. Ni, W. Bu, J. Shi, Near infrared-assisted Fenton reaction for tumor-specific and mitochondrial DNA-targeted photochemotherapy, *Biomaterials* 141 (2017) 86–95.
- [31] Y. Lyu, J. Zeng, Y. Jiang, X. Zhen, T. Wang, S. Qiu, X. Lou, M. Gao, K. Pu, Enhancing both biodegradability and efficacy of semiconducting polymer nanoparticles for photoacoustic imaging and photothermal therapy, *ACS Nano* 12 (2) (2018) 1801–1810.
- [32] J. Noh, B. Kwon, E. Han, M. Park, W. Yang, W. Cho, W. Yoo, G. Khang, D. Lee, Amplification of oxidative stress by a dual stimuli-responsive hybrid drug enhances cancer cell death, *Nat. Commun.* 6 (2015) 6907.
- [33] C. Gorrini, I.S. Harris, T.W. Mak, Modulation of oxidative stress as an anticancer strategy, *Nat. Rev. Drug Discov.* 12 (12) (2013) 931.
- [34] R.A. Cairns, I.S. Harris, T.W. Mak, Regulation of cancer cell metabolism, *Nat. Rev. Cancer* 11 (2) (2011) 85.
- [35] N. Gong, X. Ma, X. Ye, Q. Zhou, X. Chen, X. Tan, S. Yao, S. Huo, T. Zhang, S. Chen, X. Teng, X. Hu, J. Yu, Y. Gan, H. Jiang, J. Li, X.-J. Liang, Carbon-dot-supported atomically dispersed gold as a mitochondrial oxidative stress amplifier for cancer treatment, *Nat. Nanotechnol.* 14 (4) (2019) 379.
- [36] Y. Lu, Y. Yang, Z. Gu, J. Zhang, H. Song, G. Xiang, C. Yu, Glutathione-depletion mesoporous organosilica nanoparticles as a self-adjunct and Co-delivery platform for enhanced cancer immunotherapy, *Biomaterials* 175 (2018) 82–92.
- [37] L.B. Priya, R. Baskaran, C.Y. Huang, V.V. Padma, Neferine ameliorates cardiomyoblast apoptosis induced by doxorubicin: possible role in modulating NADPH oxidase/ROS-mediated NFκB redox signaling cascade, *Sci. Rep.* 7 (1) (2017) 12283.
- [38] M. Gilleron, X. Marechal, D. Montaigne, J. Franczak, R. Neviere, S. Lancel, NADPH oxidases participate to doxorubicin-induced cardiac myocyte apoptosis, *Biochem. Biophys. Res. Commun.* 388 (4) (2009) 727–731.
- [39] P.T. Yin, T. Pongkulapa, H.Y. Cho, J. Han, N.J. Pasquale, H. Rabie, J.H. Kim, J.W. Choi, K.B. Lee, Overcoming chemoresistance in cancer via combined MicroRNA therapeutics with anticancer drugs using multifunctional magnetic core-shell nanoparticles, *ACS Appl. Mater. Interfaces* 10 (32) (2018) 26954–26963.
- [40] Y. Wang, Y. Xie, J. Li, Z.H. Peng, Y. Sheinin, J. Zhou, D. Oupicky, Tumor-penetrating nanoparticles for enhanced anticancer activity of combined photodynamic and hypoxia-activated therapy, *ACS Nano* 11 (2) (2017) 2227–2238.
- [41] J. Shao, H. Xie, H. Huang, Z. Li, Z. Sun, Y. Xu, Q. Xiao, X.F. Yu, Y. Zhao, H. Zhang, H. Wang, P.K. Chu, Biodegradable black phosphorus-based nanospheres for in vivo photothermal cancer therapy, *Nat. Commun.* 7 (2016) 12967.
- [42] J. Ma, P. Li, W. Wang, S. Wang, X. Pan, F. Zhang, S. Li, S. Liu, H. Wang, G. Gao, B. Xu, Q. Yuan, H. Shen, H. Liu, Biodegradable poly(amino acid)-gold-magnetic complex with efficient endocytosis for multimodal imaging-guided chemo-photothermal therapy, *ACS Nano* 12 (9) (2018) 9022–9032.
- [43] J.H. Park, L. Gu, G. von Maltzahn, E. Ruoslahti, S.N. Bhatia, M.J. Sailor, Biodegradable luminescent porous silicon nanoparticles for in vivo applications, *Nat. Mater.* 8 (4) (2009) 331–336.
- [44] X. Ling, J. Tu, J. Wang, A. Shajii, N. Kong, C. Feng, Y. Zhang, M. Yu, T. Xie, Z. Bharwani, B.M. Aljaeid, B. Shi, W. Tao, O.C. Farokhzad, Glutathione-responsive prodrug nanoparticles for effective drug delivery and cancer therapy, *ACS Nano* 13 (1) (2018) 357–370.
- [45] R. Zhou, N. Shen, J. Zhao, Y. Su, H. Ren, Glutathione-coated Fe₃O₄ nanoparticles with enhanced Fenton-like activity at neutral pH for degrading 2,4-dichlorophenol, *J. Mater. Chem. A.* 6 (3) (2018) 1275–1283.
- [46] X. Huang, L. Li, T. Liu, N. Hao, H. Liu, D. Chen, F. Tang, The shape effect of mesoporous silica nanoparticles on biodistribution, clearance, and biocompatibility in vivo, *ACS Nano* 5 (7) (2011) 5390–5399.
- [47] T. Liu, W. Liu, M. Zhang, W. Yu, F. Gao, C. Li, S.B. Wang, J. Feng, X.Z. Zhang, Ferrous-supply-regeneration nanoengineering for cancer-cell-specific ferroptosis in combination with imaging-guided photodynamic therapy, *ACS Nano* 12 (12) (2018) 12181–12192.
- [48] J. Yu, C. Yang, J. Li, Y. Ding, L. Zhang, M.Z. Yousaf, J. Lin, R. Pang, L. Wei, L. Xu, F. Sheng, C. Li, G. Li, L. Zhao, Y. Hou, Multifunctional Fe₃C₂ nanoparticles: a targeted theranostic platform for magnetic resonance imaging and photoacoustic tomography-guided photothermal therapy, *Adv. Mater.* 26 (24) (2014) 4114–4120.
- [49] W. Tao, X. Ji, X. Zhu, L. Li, J. Wang, Y. Zhang, P.E. Saw, W. Li, N. Kong, M.A. Islam, T. Gan, X. Zeng, H. Zhang, M. Mahmoudi, G.J. Tearney, O.C. Farokhzad, Two-dimensional antimonene-based photonic nanomedicine for cancer theranostics, *Adv. Mater.* 30 (38) (2018) e1802061.
- [50] X. Ji, N. Kong, J. Wang, W. Li, Y. Xiao, S.T. Gan, Y. Zhang, Y. Li, X. Song, Q. Xiong, S. Shi, Z. Li, W. Tao, H. Zhang, L. Mei, J. Shi, A novel top-down synthesis of ultrathin 2D boron nanosheets for multimodal imaging-guided cancer therapy, *Adv. Mater.* 30 (36) (2018) e1803031.
- [51] Z. Wang, X. Xue, Y. He, Z. Lu, B. Jia, H. Wu, Y. Yuan, Y. Huang, H. Wang, H. Lu, K.S. Lam, T.-Y. Lin, Y. Li, Novel redox-responsive polymeric magnetosomes with tunable magnetic resonance property for in vivo drug release visualization and dual-modal cancer therapy, *Adv. Funct. Mater.* 28 (33) (2018) 1802159.
- [52] D. Li, Y. Ma, J. Du, W. Tao, X. Du, X. Yang, J. Wang, Tumor acidity/NIR controlled interaction of transformable nanoparticle with biological systems for cancer therapy, *Nano Lett.* 17 (5) (2017) 2871–2878.
- [53] Z. Tu, H. Qiao, Y. Yan, G. Guday, W. Chen, M. Adeli, R. Haag, Directed graphene-based nanoplatforms for hyperthermia: overcoming multiple drug resistance, *Angew. Chem. Int. Ed. Engl.* 57 (35) (2018) 11198–11202.
- [54] M. Zhou, S. Liu, Y. Jiang, H. Ma, M. Shi, Q. Wang, W. Zhong, W. Liao, M.M.Q. Xing, Doxorubicin-loaded single wall nanotube thermo-sensitive hydrogel for gastric cancer chemo-photothermal therapy, *Adv. Funct. Mater.* 25 (29) (2015) 4730–4739.
- [55] P.T. Yin, S. Shah, M. Chhowalla, K.B. Lee, Design, synthesis, and characterization of graphene-nanoparticle hybrid materials for bioapplications, *Chem. Rev.* 115 (7) (2015) 2483–2531.
- [56] J. Zeng, D. Goldfeld, Y. Xia, A plasmon-assisted optofluidic (PAOF) system for measuring the photothermal conversion efficiencies of gold nanostructures and controlling an electrical switch, *Angew. Chem. Int. Ed. Engl.* 52 (15) (2013) 4169–4173.
- [57] P. Wust, B. Hildebrandt, G. Sreenivasa, B. Rau, J. Gellermann, H. Riess, R. Felix, P.M. Schlag, Hyperthermia in combined treatment of cancer, *Lancet Oncol.* 3 (8) (2002) 487–497.
- [58] R.W. Robey, K.M. Pluchino, M.D. Hall, A.T. Fojo, S.E. Bates, M.M. Gottesman, Revisiting the role of ABC transporters in multidrug-resistant cancer, *Nat. Rev. Cancer* 18 (7) (2018) 452–464.
- [59] L. Wang, X. Lin, J. Wang, Z. Hu, Y. Ji, S. Hou, Y. Zhao, X. Wu, C. Chen, Novel insights into combating cancer chemotherapy resistance using a plasmonic nanocarrier: enhancing drug sensitiveness and accumulation simultaneously with localized mild photothermal stimulus of femtosecond pulsed laser, *Adv. Funct. Mater.* 24 (27) (2014) 4229–4239.
- [60] J. Yang, S. Zhai, H. Qin, H. Yan, D. Xing, X. Hu, NIR-controlled morphology transformation and pulsatile drug delivery based on multifunctional phototheranostic nanoparticles for photoacoustic imaging-guided photothermal-chemotherapy, *Biomaterials* 176 (2018) 1–12.
- [61] H.Y. Cho, T. Lee, J. Yoon, Z. Han, H. Rabie, K.B. Lee, W.W. Su, J.W. Choi, Magnetic oleosome as a functional lipophilic drug carrier for cancer therapy, *ACS Appl. Mater. Interfaces* 10 (11) (2018) 9301–9309.
- [62] G. Szakacs, J.K. Paterson, J.A. Ludwig, C. Booth-Genthe, M.M. Gottesman, Targeting multidrug resistance in cancer, *Nat. Rev. Drug Discov.* 5 (3) (2006) 219–234.
- [63] M. Hao, C. Kong, C. Jiang, R. Hou, X. Zhao, J. Li, Y. Wang, Y. Gao, H. Zhang, B. Yang, J. Jiang, Polydopamine-coated Au-Ag nanoparticle-guided photothermal colorectal cancer therapy through multiple cell death pathways, *Acta Biomater.* 83 (2019) 414–424.
- [64] M.C. Damien Montarnal, François Tournilhac, Ludwik Leibler, Silica-like malleable materials from permanent organic networks, *Science* 334 (6058) (2011) 965–968.
- [65] K. Welscher, S.P. Sherlock, H. Dai, Deep-tissue anatomical imaging of mice using carbon nanotube fluorophores in the second near-infrared window, *Proc. Natl. Acad. Sci. U.S.A.* 108 (22) (2011) 8943–8948.
- [66] K. Cherukula, S. Uthaman, I.-K. Park, “Navigate-dock-activate” anti-tumor strategy: tumor micromilieu charge-switchable, hierarchically activated nanoplatform with ultrarapid tumor-tropic accumulation for trackable photothermal/chemotherapy, *Theranostics* 9 (9) (2019) 2505.
- [67] L. Yang, S.-T. Chueng, Y. Li, M. Patel, C. Rathnam, G. Dey, L. Wang, L. Cai, K.-B. Lee, A biodegradable hybrid inorganic nanoscaffold for advanced stem cell therapy, *Nature Communications* 9 (2018), <https://doi.org/10.1038/s41467-018-05599-2>.